# Comparison and Validation of BEM and Free Wake Unsteady Panel Model with the MEXICO Rotor Experiment

Daniel Micallef [1,2] ,Menno Kloosterman[1], Carlos Simão Ferreira[1], Tonio Sant[2] , Gerard van Bussel[1]

November 26, 2009

**Abstract**

The Model Rotor Experiments under Controlled Conditions (MEXICO) project aimed at creating a database of wind turbine rotor aerodynamic measurements under wind tunnel controlled conditions, for validating and improving wind turbine rotor aerodynamic simulation methods.

An extensive measurement program was carried out on a three bladed 4.5m diameter rotor model in the DNW wind tunnel (open jet test cross section of 9.5 × 9.5m). The measurements consisted of pressure distribution along the chord at five spanwise locations of the blade and Stereo Particle Image Velocimetry at certain location of the flow field, including the tip vortex. The measurements included both yawed and non yawed conditions.

This work presents some of the results of the MEXICO experiment and a comparison between blade element momentum codes and free-wake unsteady potential-flow codes. The comparison is performed with results for axial and yawed flow cases, with special focus on the aerodynamic effect of yaw. Power and load curves have been obtained, including along spanwise load distribution. Experimental tip-vortex strength decay in the near wake enabled a comparison with tip vortex trajectories in the near wake obtained with the free-wake code. *Keywords: MEXICO experiment, Blade Element Momentum, Free Wake, Particle Image Velocimetry, Axial flow, Yawed flow.*

## Introduction

In the MEXICO experiment, a three bladed, 4.5m diameter rotor, with a hub diameter of 0.42m was tested in the Large Scale Low Speed (LLF) facility of the DNW using the open jet configuration which has a cross-section of 9.5 × 9.5m. The blade had a span of 2.04m. Figure 1 shows the experimental turbine in the wind tunnel. The rotation direction of the model was clockwise. The blade numbering and yaw angle definitions are shown in figure 2.

Each blade consists of three airfoils; the root region of the blade is made of a DU 91-W2-250 airfoil section, the mid-span is made of the RisøA1-21 airfoil and the tip region is made of the NACA 64-418 airfoil. The chord and twist distributions are shown in figure 3.

Kulite® pressure sensors were placed along spanwise and chordwise positions on each of the three blades. Each of the spanwise positions had between 25 to 28 sensors, more

[1]DUWIND, TUDelft, Faculty of Aerospace Engineering, Kluyverweg 1, 2629 HS, Delft, The Netherlands

[2]University of Malta, Department of Mechanical Engineering, Malta.

Figure 1: MEXICO rotor in DNW wind tunnel ready for testing.

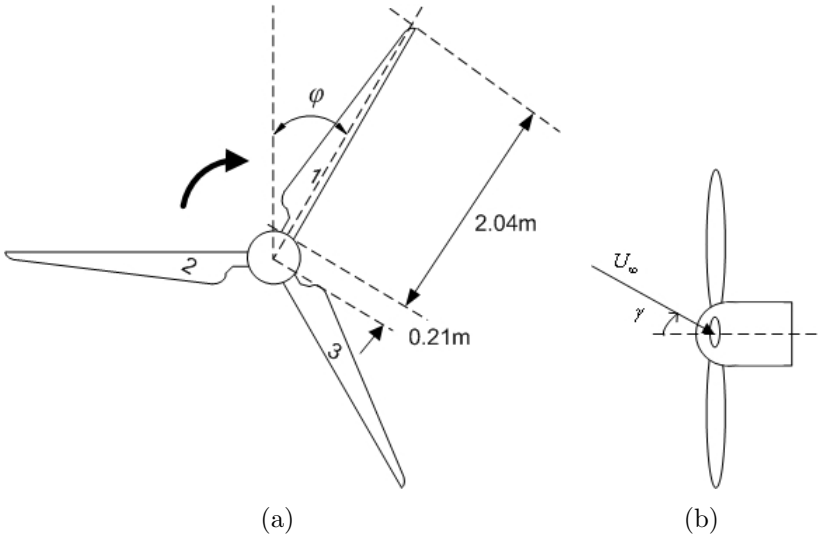


Figure 2: (a) Rotor geometry and blade numbering, (b) Yaw angle convention

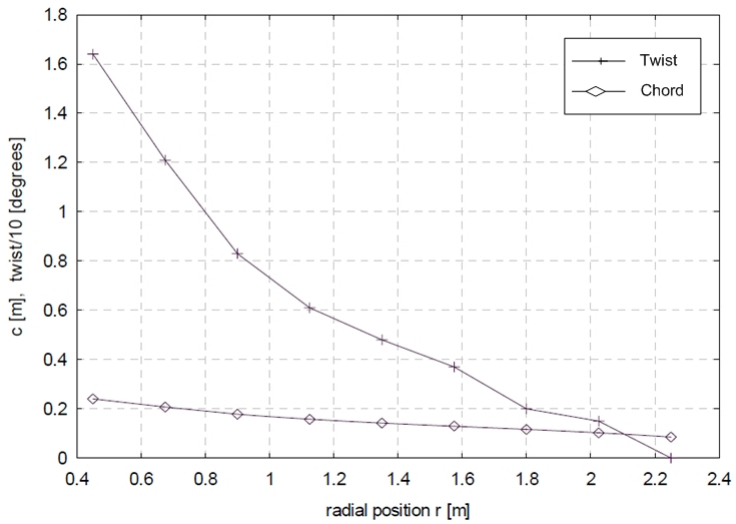


Figure 3: Chord and twist distribution.

densely packed towards the leading edge to capture the high pressure gradients occurring in this region. Figure 4 shows the locations of main measuring sensors (bold lines) and

validation sensors (regular dotted lines).

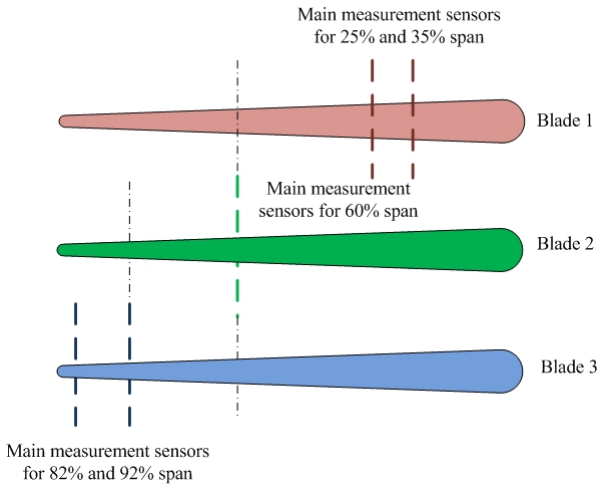


Figure 4: Sensor configuration on blades.

Measurements were taken for 27 consecutive rotor revolutions(at 325RPM) and 35 consecutive rotor revolutions (at 425RPM.). The pressure measurments for yawed flow conditions were carried out at yaw angles of 15, 30 and 45 degrees. Particle Image Velocimetry (PIV) data was gathered and during these PIV tests, pressure readings where registered. The major aim of the PIV data was tip vortex tracking. Most of the readings in this case were taken for axial flow. The only PIV data taken for yawed flow are for $\pm 30^o$ yaw and 15m/s. Parked rotor as well as dynamic inflow measurements were also taken but these will not be considered further in this work [1], [2], [3].

**Experimental Data Validation**

A validation study of the MEXICO data is carried out. When mean readings are compared for the sensors used for validation purposes (see fig. 4), some discrepancies are observed. After performing tests for normality using quantile-quantile plots, hypothesis tests for differences between means with 95% confidence were performed but most of the hypotheses were rejected. Although it was apparent that there is a certain level of disagreement between results, the cause of such a disagreement is yet unclear. Figure 5 shows an example of differences in pressure coefficient obtained from sensors which are supposedly measuring the same value.

Possible causes of this error could be either a geometrical offset or a signal offset from the sensors. In many cases, the discrepancy which results in the pressure coefficient distributions was very small. The largest errors occur on the 60% span position at low tip speed ratio cases (from figure 5 the maximum difference in $C_p$ is around 0.1). The readings from the main measuring blades were used in the current analysis. In cases of malfunctioning sensors showing no signal, readings from validation sensors were utilized. For the load calculations, an uncertainty analysis on sensor positions was performed. A cubic interpolation provided the best results and was hence used.

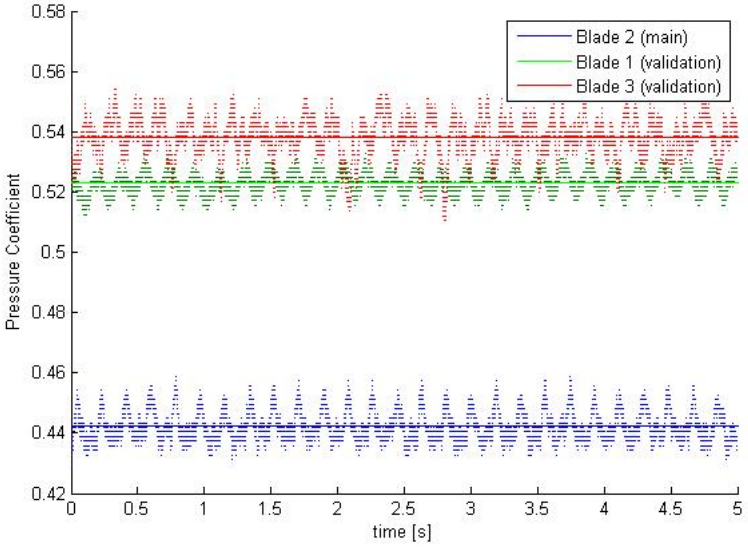


Figure 5: Differences in pressure coefficient between sensors used for validation purposes on all three blades at 60% span and 13% fraction of chord. Axial flow, wind speed of 13.07m/s and rotor speed of 324.3RPM. The quantities have been non-dimensionalized by the maximum pressure measurement.

### BEM Model Features

The Blade Element Momentum (BEM) model will now be presented along with its validation.

Two corrections were implemented: a Prandtl tip loss factor correction model and a turbulent wake state correction model. In this work it was opted to rely on the Prandtl tip loss factor developed by Ludwig Prandtl in 1919 [6]. Recently there have been various attempts to improve on the Prandtl tip loss model [4]. CFD techniques have also been effectively used for better prediction of the inductions at the rotor [5]. These however rely on empirical data and in this work it was opted to rely on the original Prandtl tip loss factor. This original correction was validated extensively and used with other BEM models such as AeroDyn [7]. This Prandtl tip loss model accounts for the tip effect only and it has therefore been extended to incorporate the effect of the root.

For a turbulent wake state correction, which occurs at high axial thrust coefficients and hence at high tip speed ratios, the condition was taken as $a_T > 0.45$ as this provided the best agreement with experimental data. If an empirical line is passed through the position defined by $a_T$ and through a point defined at an induction factor of 1 called $C_{T1}$ then this line has the equation [6]:

$$C_T = C_{T1} - 4(\sqrt{(C_{T1} - 1)}(1 - a_1) \tag{1}$$

The value of the thrust coefficient at the stated transition point is:

$$C_{T1} = 4(1 - a_T)^2 \tag{2}$$

In this case eqn. 2 gives $C_{T1} = 1.21$. This transition point is rather empirical and must therefore be chosen carefully to ensure that the results coincide well with the experimental ones. The transition point was chosen since it provided the most reasonable

value which matched the experimental data. One must however note that modification of this parameter might be necessary to yield correct results in high tip speed ratio cases.

For the yaw model, no turbulent wake correction is made. The model follows the same methodology as given in [6]. Both flow expansion as well as wake rotation were taken into account. The flow expansion function was taken as that proposed by Øye [8]:

$$F(\mu) = \frac{1}{2}(\mu + 0.4\mu^3 + 0.4\mu^5) \tag{3}$$

In the theory of Glauert [9], the azimuthally averaged induction is assumed constant. The induced velocity in yaw would then be given by:

$$u = u_{avg}(1 + K(\chi)F(\mu)sin\psi) \tag{4}$$

The function $K(\chi)$ depends on the wake shape. There are a number of models [10] for this function but in this work the Pitt and Peters model [11] is used:

$$K(\chi) = \frac{15\pi}{32}tan\frac{\chi}{2} \tag{5}$$

This BEM model has been validated with experiment. It uses 2D airfoil data for all the three airfoil sections, DU 91-W2-250, RisøA1-21 and NACA 64-418 airfoils respectively. Hence, by comparing results from BEM with experiment the validity of using such airfoil data may be checked thoroughly.

## BEM Model Validation

For axial flow conditions, close agreement with the data was expected since BEM has been extensively validated in the past [7]. Comparisons were made with the measurements obtained by means of the Kulite® sensors placed on the entire blade span. The blade load distributions from the experiment were obtained by means of pressure integration. It must be noted that strain gauge data was also gathered during the experiment. In the calculation of the torque, however, strong discrepancies were found and hence the strain gauge results were not used further.

### *Axial Flow*

The comparison between rotor thrust coefficient and power curve as obtained from the BEM code and from experimental measurements are shown in figure 6 and 7. For the thrust coefficient against tip speed ratio at low rotor speed there is quite a good agreement between all curves at low and high tip speed ratio. The highest difference between the results is at around $\lambda = 8$. At the higher TSR values, for both rotor speed, the agreement is worse. The power curves show very good agreement at low wind speeds but not at high wind speeds. The experimental prediction shows a maximum in the 325RPM case which is not predicted by the BEM model. This is probably due to stall delay effect which the BEM model does not account for. In a validation study for a helicoidal vortex model with the NREL Unsteady Aerodynamics Experiment, a similar problem was found by M.Hallisy *et al* [12]. This discrepancy is therefore not only limited to BEM models.

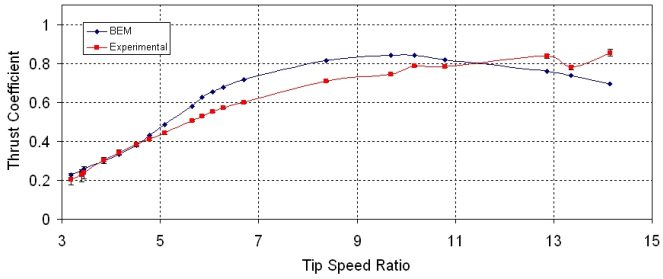


Figure 6: Thrust coefficient against tip speed ratio for a rotor speed of 325RPM and pitch of -2.3 degrees

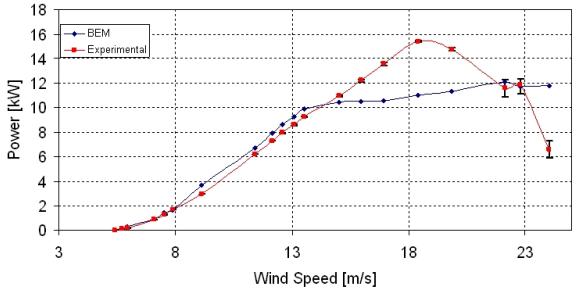


Figure 7: Power curve for a rotor speed of 325RPM and pitch of -2.3 degrees

Various other results have been derived but are not shown here. For instance, the power coefficient against TSR curves were obtained and showed acceptable agreement. The BEM model however gives some discrepancies related to the maximum power coefficient. The reader is referred to [13].

### *Yawed Flow*

For the validation of the BEM yaw model both loading and power prediction are again considered. Figure 8 shows normalized power predictions for 30 degree yaw as predicted by BEM and experiment. The model performs acceptably well at low TSR. For a high TSR, the discrepancy between BEM and experiment is large. The reason for may be due to the higher unsteadiness which occurs at these tip speed ratios. In fact, an estimate for the reduced frequency may be given by [18]:

$$k = \frac{\Omega c}{2\left(\Omega r + U_\infty sin\gamma\right)} = \left(\frac{1}{r/R + sin\gamma/\lambda}\right)\frac{c}{2R} \tag{6}$$

Hence, the higher the tip speed ratio, the higher the reduced frequency and hence the unsteadiness.

## Stagnation Pressure Analysis

The stagnation pressure variation for both axial and yawed flow could yield important information. The BEM model for both flow cases was designed by only using the simplest

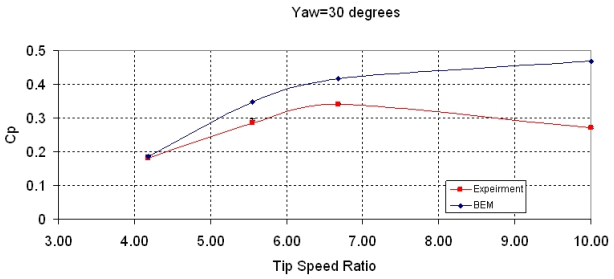


Figure 8: Power coefficient for 30 degree yaw from experiment and from BEM.

correction models. In particular no correction was made to effects such as stall delay. There are a number of stall delay models which can be adopted in a BEM approach. These have been validated in the past and compared with experiment such as the NREL Phase VI experimental data [14].

By tracking the discrepancies from experimental data, one can decipher why these discrepancies take place. It must be noted that the stagnation pressure for the experimental data is taken as the maximum pressure reading from all of the sensors at a particular airfoil section. This pressure is not the real stagnation pressure since there are high pressure gradients occurring in this location. So the data was interpolated using cubic hermite polynomials and spline interpolation to try to obtain a better value of the stagnation pressure. This interpolation study resulted in only a small difference between the measured maximum and the interpolated value.

The stagnation pressure from the BEM model is taken as the dynamic pressure:

$$p_{stag} = \frac{1}{2}\rho V_{rel}^2 \tag{7}$$

where $\rho$ =air density, and $V_{rel}$ is the relative velocity.

The percentage discrepancies between the predictions of the BEM model and the experimental values are plotted for the axial flow case for various TSRs. This percentage discrepancy was calculated from:

$$\%\Delta = \left| \frac{p_{BEM} - p_{exp}}{p_{exp}} \right| \times 100 \tag{8}$$

For both speeds the greatest percentage difference occurs towards the root of the blade at the 25% and 35% stations. There is no clear trend on the variation of this quantity with TSR. The low rotational speed case of 325RPM is shown in figure 9. At the 60% station there is a clear reduction in the percentage difference between model and experiment which is around 20%. At the 82% and 92% outboard stations the percentage differences reduce even further to around 10%. Three major reasons can be deduced to explain the differences in results. Since no stall delay model is used to correct for the two-dimensional airfoil data, the large percentage error in the root region of the blade was expected. The effects of stall delay are attenuated towards the tip of the blade. Agreement in this region is better. The measurement of the stagnation pressure on the blade (taken as the maximum pressure reading over the airfoil) is rather inaccurate due to high pressure gradients at the leading edge. Finally, the dynamic pressure as calculated from BEM is calculated based on the relative velocity calculated at a nominal radius at which the (0.25c) airfoil rotates and not the radius at the leading edge.

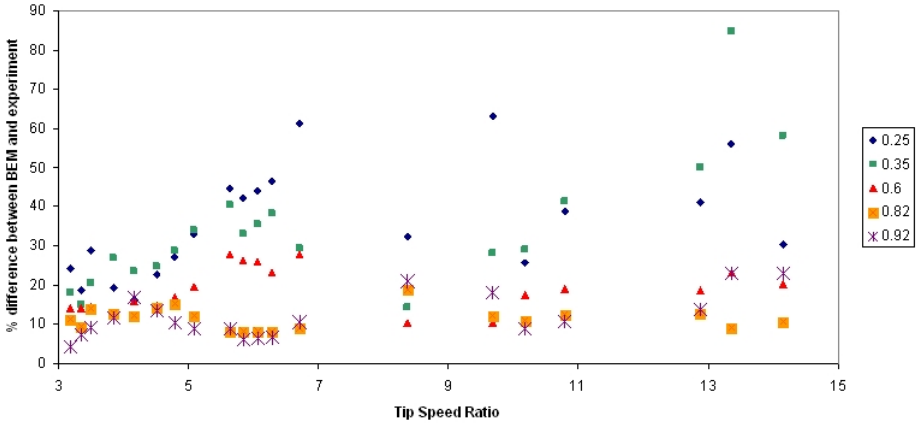


Figure 9: Stagnation pressure percentage difference between BEM and experiment for a rotor speed of 325RPM at various span wise stations and at $\psi = 0^o$.

### Three Dimensional Airfoil Data

For axial conditions there is no cyclic variations of the angle of attack with azimuth. For this reason it is possible to isolate the effects of three dimensionality from the unsteady effects. Three dimensional airfoil data may therefore be extracted. This data will however depend on the rotational speed of the rotor. The higher the speed, the higher the stall delay since centrifugal forces on the air towards the inboard sections allows for improved boundary layer stability. The 3D lift and drag coefficients are compared with their 2D counterparts for different angles of attack. The blade element momentum approach, by means of the 2D static airfoil data enables the determination of the angle of attack. In the proposed simulation, no account is taken for 3D effects and for the effects of unsteadiness especially in yawed flow. There is therefore an inherent difficulty in calculating angles of attack. However, through these estimates of the angle of attack, one can obtain the lift and drag coefficient versus AOA based on the loading which is gathered from the experiment. Thus, from the normal and tangential loads $N$ and $A$ and through the determination of the AOA $\alpha$ from BEM (based on 2D data input) the lift and drag may be established as follows:

$$L = Ncos\alpha - Asin\alpha \tag{9}$$

$$D = Nsin\alpha + Acos\alpha \tag{10}$$

Note that the sign convention taken here corresponds to that taken for the experimental data. The positive $x$ axis goes from the airfoil leading edge towards the trailing edge while the positive y axis is on the low pressure side. From these, the lift and drag coefficients can be found from:

$$C_L = \frac{L}{\frac{1}{2}\rho V_{rel}^2} \tag{11}$$

$$C_D = \frac{D}{\frac{1}{2}\rho V_{rel}^2} \tag{12}$$

The dynamic pressure in the denominator is taken as the maximum pressure measured over the airfoil corresponding to a hypothetical maximum. Previously it was shown that through interpolation there is only a very slight variation from this maximum.

To obtain the $C_L - \alpha$ and $C_D - \alpha$ data various data points with different wind speeds where considered for a constant pitch of -2.3 degrees. This enabled different angles of attack for different spanwise stations to be obtained. The corresponding lift and drag coefficients were then obtained from the experimental loads. In figure 10 the lift and drag coefficients are shown for the 25% and 35% span locations. It is clear that stall delay affects the inner part of the rotor since the 25% and 35% stations show a higher lift coefficient even above the 2D stall angle. However, it may also be observed that for the 324.5RPM case, the 35% station is less affected by stall delay and stall occurs more or less in the region close to the 2D static stall angle. For this same case the maximum lift coefficient attained by the 25% station is around 1.6 compared to a 2D maximum of around 1.2. At the high rotational speed of 424.5RPM (not shown here) the 35% station is also affected dramatically by stall delay. The range of data which is available for this case does not include higher angles of attack than is necessary to determine a maximum lift. At the 25% station however a lift coefficient of around 1.8 is reached while at the 35% station a maximum lift of around 1.6 is reached. At the 60% span position the lift is for the most part lower than the 2D case. This must be due to the tip loss effect which is modeled in BEM, an effect which was also observed by using an inverse free wake vortex model with the NREL UAE experimental data as input [15]. The lift however continues to increase above the static stall angle and yet the lift at this point is only slightly larger than the stall 2D airfoil. At a higher rotational speed the lift is very slightly enhanced showing that stall delay is not affecting much this station. The tip loss effect therefore seems to shift the lift curve downwards but also slightly delaying stall. At the 82% station for low rotational speed we have a similar sitatuation as the 60% case without stall. The loss of lift here is more prevalent and is always below the static 2D data even above stall conditions. The high rotational speed case doesn't vary much from the low speed case. At the 92% station there is an even greater loss of lift due to the strong tip vortices affecting this region. It is very interesting to note that at this position the lift coefficient is always smaller than the static 2D data. This effect was also observed in the NREL UAE experiment [15]. The drammatic drop in lift occurs at a much higher angle of attack indicating stalled conditions. This supports further the idea that the tip effect reduces lift but enables better boundary layer stability. This hypothesis is not possible for the high speed case as not enough high angle of attack data points are present. For more information the reader is again referred to [13].

When the rotor has some yaw error, unsteadiness is induced as the rotor rotates in a cyclic manner. In consequence to this, the angle of attack will vary with azimuth.

If the reduced frequency (as defined by defined by 6) is in the range $0 \leq k \leq 0.02$ the situation may be considered steady. If $k \geq 0.2$ then the situation is highly unsteady and the BEM model is most likely to give erroneous results as no account is taken for this unsteadiness [16]. In figure 11 the lift and drag coefficients are plotted against angle of attack. The third diagram represents the reduced frequency variation with azimuth. On these diagrams, the green circle represents the 0.02 limit below which the situation can be considered steady. The red line indicates the value of $k$ as it varies with azimuth. For

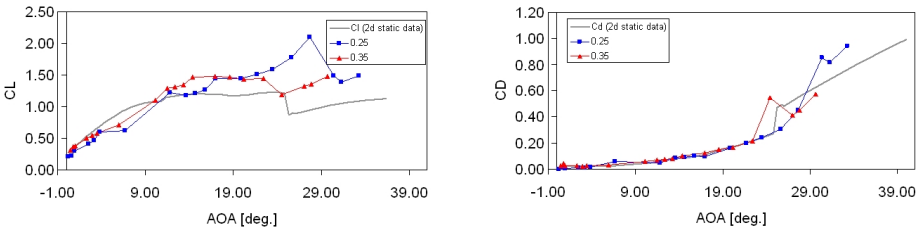


(a) $C_L - \alpha$ (b) $C_D - \alpha$

Figure 10: Lift coefficient against angle of attack for a rotational speed of 325RPM at the 25% and 35% spanwise locations corresponding to the DU91-W2-250 (a) $C_L$ against $\alpha$, (b) $C_D$ against $\alpha$

quasi-steady flow, the red line must lye within the green circle.

At the highest tested wind speed of 24m/s (shown in figure 11) the flow may be considered for the most part unsteady for the 25, 35 and 60% stations. The 82% station shows also some unsteadiness but to a much lower extent. Unfortunately this is not captured in the BEM derived loops since they are still relatively wide. At the 25% and 35% positions, hints of dynamic stall are present as a dramatic drop in lift is observed. The lift coefficients obtained at all stations are mostly smaller than the 2D static curve but show higher maximum lifts. The drag coefficients are lower than the 2D quantities and are sometimes negative. As in the axial flow case, at outboard stations, a loss of lift can be observed even though the flow approaches steady behaviour.

### Comparison Between Direct Free Wake Model and MEXICO Results

A direct free wake potential model is developed and validated with wind tunnel hot-film measurements, MEXICO PIV data as well as with other validated free wake codes. The model uses a lifting line approach. This involves an iterative process to calculate the bound vorticity. This is done by equating the lift due to the circulation found from the effective angle of attack for every blade section. This is repeated until a user defined convergence criterion is obtained. From the bound circulation the induced velocities may be determined. An Euler scheme was implemented to find the wake nodes displacement. This method requires the input of 2D airfoil data as was the case with the BEM approach.

Verification of the model was done with respect to the number of blade nodes, azimuthal step as well as number of revolutions. The $R^2$-norm was used to obtain as single value of the percentage error which is given by:

$$\epsilon = \left| \frac{\xi_i - \xi_{ref}}{\xi_{ref}} \right| \tag{13}$$

$$\epsilon_{R^2} = \sqrt{\frac{\sum_{i=1}^{N} \epsilon_i}{N}} \tag{14}$$

The validation of this model with respect to the MEXICO experiment was based solely on vortex tracking using the PIV data for axial flow. Further work needs to be performed for validation in yawed flow. Since the MEXICO rotor is three bladed, the age difference

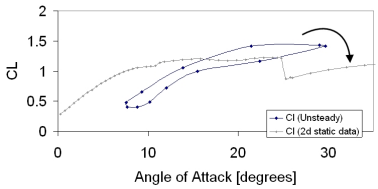


(a) $C_L - \alpha$, 25% span

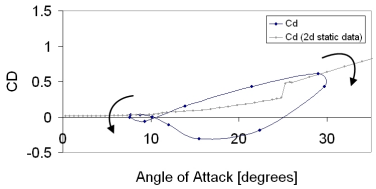


(b) $C_D - \alpha$, 25% span

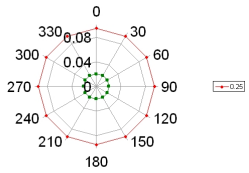

(c) Reduced frequency, 25% span

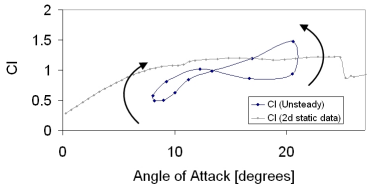


(d) $C_L - \alpha$, 35% span

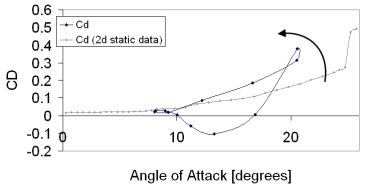


(e) $C_D - \alpha$, 35% span

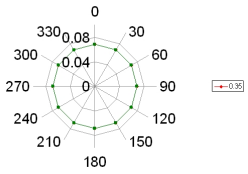

(f) Reduced frequency, 35% span

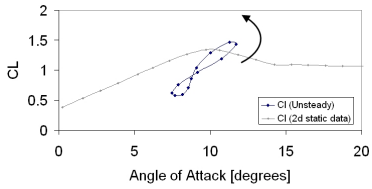


(g) $C_L - \alpha$, 60% span

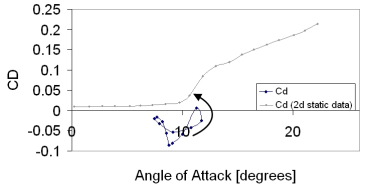


(h) $C_D - \alpha$, 60% span

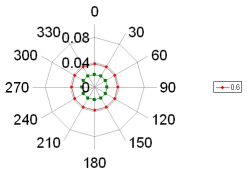

(i) Reduced frequency, 60% span

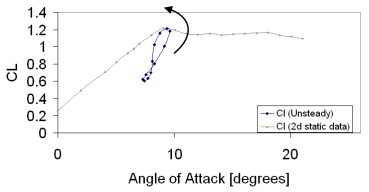


(j) $C_L - \alpha$, 82% span

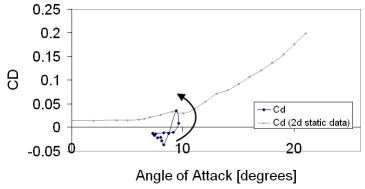


(k) $C_D - \alpha$, 60% span

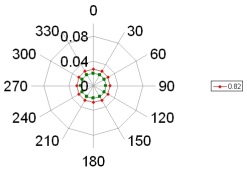

(l) Reduced frequency, 82% span

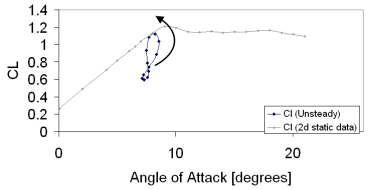


(m) $C_L - \alpha$, 92% span

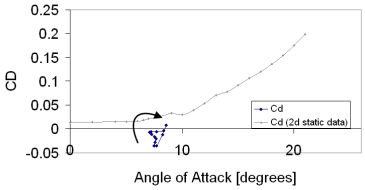


(n) $C_D - \alpha$, 92% span

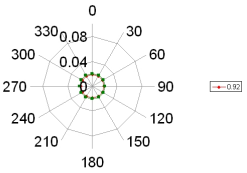

(o) Reduced frequency, 92% span

Figure 11: $C_L - \alpha$, $C_D - \alpha$ and reduced frequency for a wind speed of $U_\infty = 24m/s$ and a rotor speed of 424.5RPM and a constant pitch of -2.3 degrees, yaw angle = 45 degrees

between successive vortices is $120^o$. Especially the plots of the vorticity allow an easy identification of the vortex core since this region typically contains very high vorticity whereas the flow outside the core is much more reminiscent of the classical potential vortex flow. Although the measurements were taken every one third of a revolution, interpolation could be performed for the position and strength of the tip vortex. For a more detailed description of the interpolation algorithm the reader is referred to [17]. The tip vortex evolution from experiment is shown in figure 12.

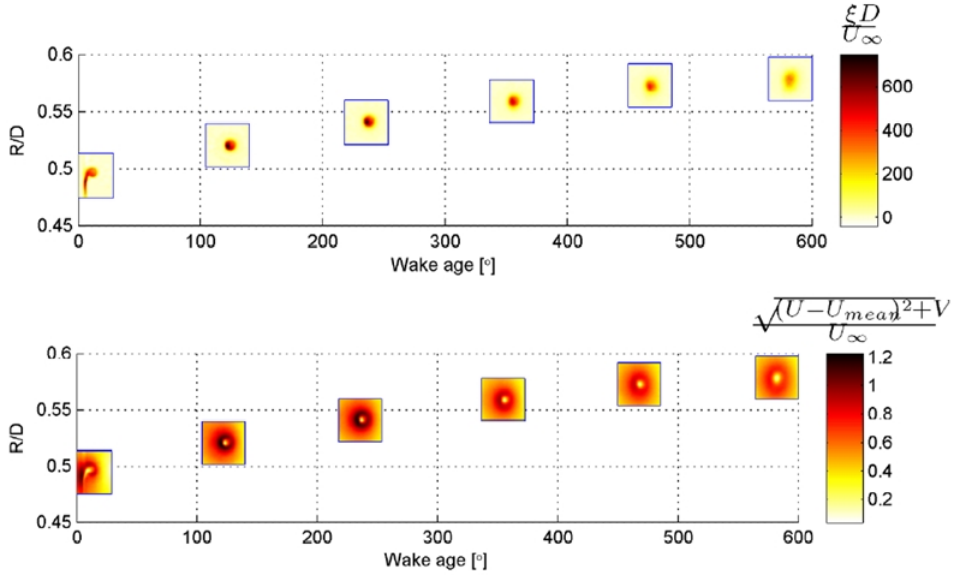


(a) Experimental result

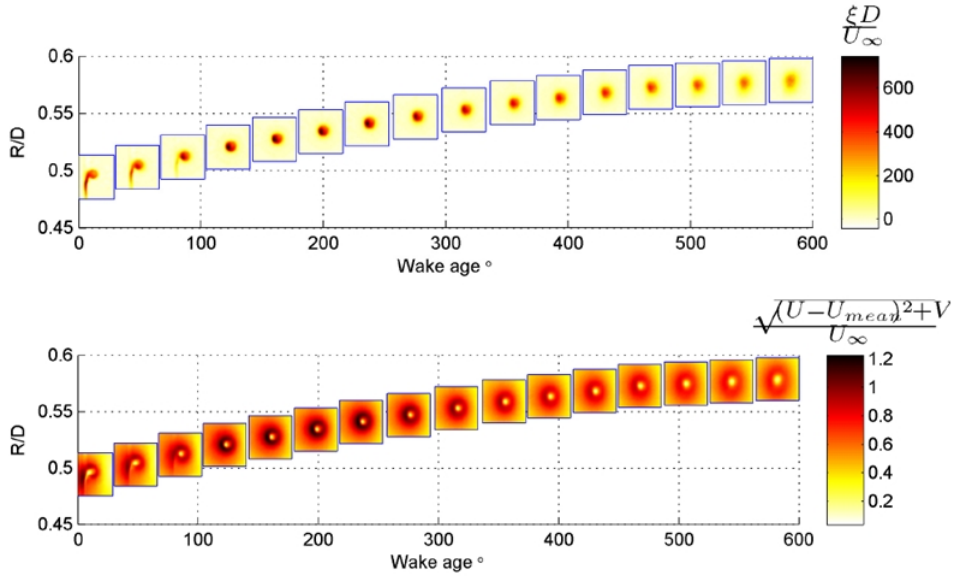


(b) Interpolated result

Figure 12: Vortex evolution from experiment and by using an interpolation algorithm (a) experiment, (b) interpolated results.

To compare the vortex evolution the interpolated data could be transformed in terms of positions and in-plane velocities to the global coordinate system. If the vorticity quantities are used, this would yield a 3D iso-vorticity plot which can be compared with the result

obtained by means of the direct free wake model. This is shown in 13. The position of the vortex is captured relatively accurately.

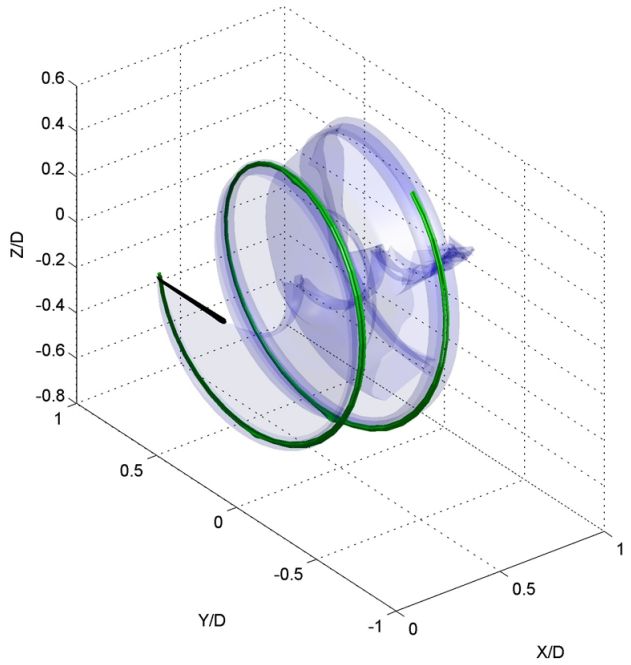


Figure 13: 3D isovorticity plot comparison between results of the direct free wake model (blue) and experiment (green).

A comparison of the vortex positions from the PIV measurements and the simulation are shown in figure 14. The vortex core positions obtained from PIV are shown in black and agree quite well with those obtained from the free vortex model. Comparisons were also made between the flow field prediction of the free wake and PIV measurements. In the free vortex code, the tip vortex is represented by means of a number of trailing votices which roll around each other.

Unfortunately, the resulting flow field is quite different from that obtained from experiment. Rather than a single tip vortex, the simulation results in a number of seperate vortices. Decreasing the mesh size did not improve results. Figure 15 shows this comparison. A second order time integration scheme instead of an Euler scheme was proposed in [17].

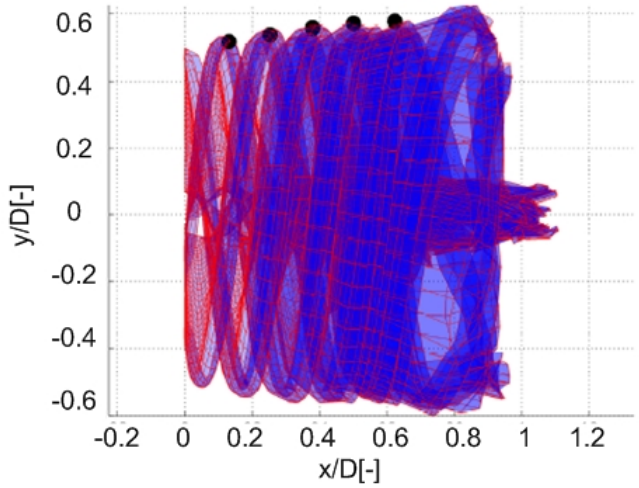


Figure 14: Vortex core positions for $C_T = 0.82$ and $\lambda = 6.7$.

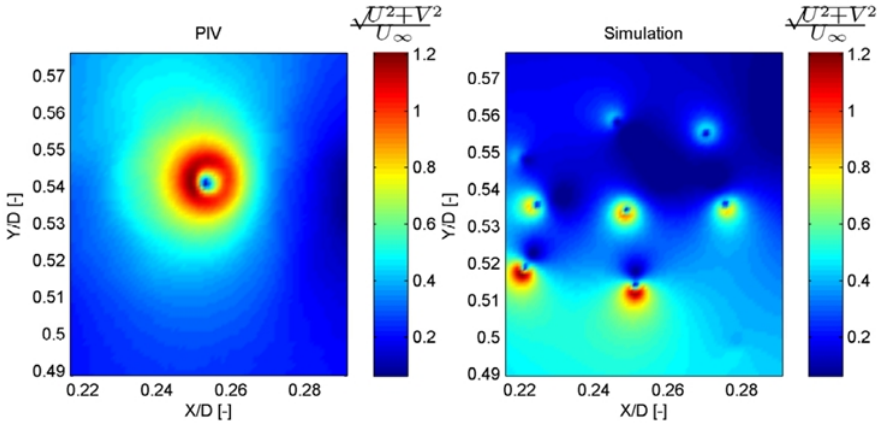


Figure 15: Comparison of simulated and measured induced velocities with $N_\phi = 50$, $N_b = 40$ and $N_{rev} = 5$.

**Acknowledgements**

The authors would like to thank Herman Snel, Gerard Schepers, Koen Boorsma and Lucas Pascal from ECN for their input in this work regarding the MEXICO data. The research work disclosed in this publication is partially funded by Malta Government Scholarship Scheme grant number MGSS PHD 2008-11.

**Nomenclature**

$U_\infty$ = Free wind speed (m/s)
$\varphi$ = Azimuth angle (degrees)
$c_p$ = Pressure coefficient
$\gamma$ = Yaw angle (degrees)
$R_t$ = Rotor tip radius (m)
$R_h$ = Rotor hub radius (m)
$r$ = elemental radius (m)

$\phi$ = Inflow angle (radians)
$f_{tip}$ = Tip loss factor
$f_{root}$ = Root loss factor
$F$ = Total tip/root loss factor
$C_T$ = Thrust coefficient
$C_{T1}$ = Thrust coefficient at an axial induction factor of 1
$C_P$ = Power Coefficient
$a_T$ = Axial induction factor at transition to turbulent wake state
$a_1$ = Axial induction factor
$F(\mu)$ = Flow expansion function
$\mu = r/R_t$ = Fraction radius
$u$ = axial velocity (m/s)
$u_{avg}$ = Average induced velocity (m/s)
$K(\chi)$ = Wake shape function
$\chi$ = Skew angle (radians)
$\lambda$ = Tip speed ratio = $R_t\Omega/U_\infty$ = TSR
$p_{stag}$ = Stagnation pressure (Pa)
$\rho$ = Air density (kg/$m^3$)
$V_{rel}$ = Relative velocity of the air to the blade (m/s)
$\Delta$ = Percentage discrepancy between BEM and experiment
$p_{BEM}$ = Dynamic pressure obtained from BEM (Pa)
$p_{exp}$ = Stagnation pressure obtained by experiment (Pa)
$L$ = Lift force per unit span (N/m)
$N$ = Normal force per unit span (N/m)
$A$ = Tangential force per unit span (N/m)
$\alpha$ = Angle of attack (degrees)
$D$ = Drag force per unit span (N/m)
$C_L$ = Lift coefficient
$C_D$ = Drag coefficient
$k$ = Reduced frequency
$\Omega$ = Rotor rotational speed (rad/s)
$c$ = Chord (m)
$N_b$ = Number of blade nodes
$N_\phi$ = Number of azimuthal steps
$N_{rev}$ = Number of consecutive rotor revolutions
$\xi_i$ = Quantity of interest for percentage error calculation
$\xi_{ref}$ = Reference quantity of interest
$\epsilon_i$ = Relative difference between qunatity of interest and the reference quantity
$\epsilon_{R^2}$ = $R^2$-norm of relative difference
$\xi$ = Vorticity ($s^{-1}$)
$D$ = Rotor diameter (m)

# References

1. *Model Experiments in Controlled Conditions(MEXICO)* - Final Report

2. K. Boorsma, J.G. Schepers *Description of experimental setup MEXICO measurements, ECN-X–09-0XX.*

3. L. Pascal, *Analysis of Mexico measurements*- ECN Wind Memo-09-010

4. W.Z. Shen, R. Mikkelsen, J.N. Sorensen and C. Bak, *Validation of Tip Corrections For Wind Turbine Computations* - EWEC 2003 Madrid.

5. W.Z.Shen, J.N.Sorensen and R. Mikkelsen, *Tip Loss Correction for Actautor/Navier-Stokes Computations*

6. T. Burton, D. Sharpe, N.Jenkins, E. Bossanyi *Wind Energy Handbook*, Wiley, 2001.

7. P.J. Moriarty, A.C. Hansen, *AeroDyn Theory Manual*, NREL (National Renewable Energy Laboratory), NREL/EL-500-36881, 2005

8. Øye, *Induced Velocities for Rotors in Yaw*, Proceedings of the Sixth IEA Symposium. ECN, Petten, Hoilland, 1992.

9. Glauert H., *A General Theory for the Autogyro*, ARC R&M 786, 1926.

10. T. Sant, *Improving BEM based Aerodynamic Models in Wind Turbine Design Codes* - PhD Dissertation, TUDelft/University of Malta

11. Pitt D.M. and Peters D.A.,*Theoretical prediction of dynamic inflow derivatives*, Vertica, 5, 21-34, 1981

12. M.Hallissy, J-J. Chattot,*Validation of a Helicoidal Vortex Model with the NREL Unsteady Aerodynamic Experiment* - AIAA-2005-1454, 2005.

13. D. Micallef: MEXICO Data Analysis, Stage III - BEM Codes Assesment, ECN.

14. S.P. Breton, F.N. Coton, G. Moe, *A Study on Rotational Effects and Different Stall Delay Models Using a Prescribed Wake Vortex Scheme and NREL Phase VI Experiment Data* - Wind Energy 2008, 11:459-482

15. T. Sant, G. van Kuik, G.J.W. van Bussel, *Estimating the Angle of Attack from Blade Pressure Measurements on the National Renewable Energy Laboratory Phase VI Rotor Using a Free Wake Vortex Model: Axial Conditions*, Wind Energy, 2006. DOI 10.1002/we.201. pgs. 549-557.

16. T. Sant, G. van Kuik, G.J.W. van Bussel, *Estimating the Angle of Attack from Blade Pressure Measurements on the National Renewable Energy Laboratory Phase VI Rotor Using a Free Wake Vortex Model: Yawed Conditions*, Wind Energy, 2009. DOI 10.1002/we.280. pgs. 1-32

17. M.H.M. Kloosterman, *Development of the Near Wake behind a Horizontal Axis Wind Turbine Including the development of a Free Wake Lifting Line Code* - M.Sc Dissertation, TUDelft.

18. J.G. Leishman, *Principles of Helicopter Aerodynamics*, Cambridge University Press, 2008.